EGTRIB Journal
JOURNAL OF
THE EGYPTIAN SOCIETY OF TRIBOLOGY
VOLUME 21, No. 4, October 2024, pp. 109 - 134 **ISSN 2090 - 5882**

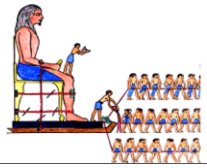

(Received July 28. 2024, Accepted in final form August 24. 2024) **jest.journals.ekb.eg**

ADHESIVE WEAR PREDICTION THROUGH FINITE ELEMENT ANALYSIS IN TRIBOLOGICAL APPLICATIONS

Mohamed H. El-shazly and Shenouda A. Zaki

Department of Mechanical Design and Production Engineering, Cairo University, Giza, EGYPT.

ABSTRACT

Adhesive wear significantly impacts the performance and longevity of dynamic systems. This study utilizes the finite element method (FEM) to simulate adhesive wear in a pin-on-disc system and calculate the wear volume. Two predictive models are used: Archard's equation and an asperity-level model. Both models are validated against experimental data. Archard's model predicts a higher wear rate, demonstrating a linear relationship between wear volume and load. In contrast, the asperity-level model reveals a non-linear relationship, offering detailed insights into wear and friction mechanisms, particularly the interplay between wear and surface roughness. However, it tends to overestimate static friction coefficients. Archard's more straightforward and user-friendly model is more appropriate for complex systems, providing practical estimates of wear volume.

KEYWORDS

Adhesive wear, asperity, finite element method, ARCARD model, tribology, pin on disc.

INTRODUCTION

Wear in dynamic systems profoundly impacts performance, efficiency, operational costs, and safety, making accurate wear prediction crucial for assessing system reliability and durability. Predicting wear through computer simulations, empirical data, or theoretical frameworks is essential for effective maintenance and design strategies. According to Burwell and John, [1], the primary wear mechanisms are abrasive, adhesive, corrosive, and fatigue wear. Abrasive wear occurs when a hard particle indents a softer surface, generating cutting grooves, while adhesive wear happens when two rough surfaces press together, causing their asperities to interlock. As the load increases, more asperities come into contact, reducing the real contact area to a fraction of the apparent area, typically ranging from 1 to 10 percent, [2, 3] .This results in the formation of a cold-welded junction whose strength is relative to the yield strength of the softer material, [4]. According to the fundamental adhesive theory of K.L. Johnson et al., [5], and Prokopovich and Victor, [6], when the surfaces move tangentially relative to each other, the adhesive junction either breaks down or small parts of the softer material are removed, depending on the junction's strength.

As tangential load increases, the junction area grows until it reaches a critical limit, beyond which sliding occurs and the junction fails or material is removed. Junction growth can exceed 60% just before slipping, with mean contact pressure decreasing once sliding begins, [7]. J. Archard's model, [8], demonstrated that wear volume is proportional to the load, sliding distance, and real contact area, with an empirically determined proportionality coefficient. Wear is influenced by the mating surface topology, which depends on the manufacturing process, contact characteristics, [9], and the properties of the rubbing surfaces rather than specific material properties. Additionally, Tabor emphasized that hardness, influenced by material composition and surface treatment, is crucial for wear resistance, [10].

Effective wear modeling is essential for predicting and mitigating wear in dynamic systems. By employing advanced modeling techniques, such as finite element analysis (FEA), engineers can simulate wear processes under various operating conditions, leading to better understanding and optimizing system performance. Accurate wear models help design more durable components, improve maintenance schedules, and reduce operational costs, ultimately enhancing the safety and efficiency of dynamic systems.

Adhesive wear modeling approaches
Haibo et al., [11], reviewed various wear modeling methods, noting that these approaches can be classified based on their macro, micro, or atomic scale. Wear modeling methods generally fall into phenomenological approaches and real contact condition models. Phenomenological approaches rely on physical understanding and experimental observation at the macro level. These models, such as Archard's theory, [8] and Rabinowicz's criterion, [12], are based on empirical coefficients and assumptions. While they can provide accurate predictions within specific operational ranges, they are limited by their assumptions and the empirical nature of their coefficients, which may not generalize well across different conditions.

In contrast, models focusing on real contact conditions, such as asperity contact models, use advanced numerical techniques to simulate wear at the micro- or atomic scale. These models operate under more relaxed assumptions and aim to reflect more realistic conditions. They offer detailed insights into wear processes by considering the actual surface characteristics and material behavior. Although they require complex calculations and accurate surface data, these models can provide more precise wear predictions by capturing the finer contact details and frictional interactions. The following section will delve into microscale modeling techniques, which are crucial for understanding adhesive wear at a more granular level.

Asperity level approach

Asperity-level models for wear prediction offer valuable insights into wear phenomena, including wear volume and particle morphology. A prominent model in this area is the Greenwood-Williamson (GW) model, [13], which analyzes contact between rough, deformable surfaces by assuming each asperity is independently

loaded. This model characterizes asperities as hemispherical with a constant radius of curvature and distributes them at varying heights over a mean surface. Subsequent research by D. Cohen et al. [14], further explored asperity interactions.

Numerical methods like the Finite Element Method (FEM) and Boundary Element Method (BEM) are extensively used to analyze complex dynamic systems. These methods transform model geometries into finite elements or boundaries, respectively, to study surface contacts. FEM, in particular, is applied to rough surface contact studies, such as those conducted by Hu et al., [15], who developed asperity-level models to evaluate contact responses. One key advantage of asperity modeling is its ability to assess wear particle formation. For example, H. Zhang and I. Etsion, [16, 17], employed FEM to investigate spherical contact and adhesion wear, focusing on friction coefficients and wear volume for both elastic and plastic deformations.

On a smaller scale, atomic-level contact models provide detailed insights into wear processes but are limited by their computational demands. Researchers like J. François et al., [18] used BEM to study atomic-scale asperity contact, finding that junction growth is crucial for wear particle formation. However, these models often require very dense meshes, which can restrict their practical application. Additionally, asperity models must include criteria for crack initiation and propagation to simulate surface fracture effectively, as demonstrated, [17, 19]. They also need material models for plastic flow, requiring empirical coefficients, [20, 21].

MODELING APPROACHES

Pin on disc modeling

The pin-on-disc apparatus measures the wear volume between a pair of materials. Typically, this setup involves a pin made of a softer material loaded vertically onto a rotating disc made of a more rigid material. The disc rotates at a specified angular speed, and wear is assessed by measuring the loss in the pin's weight, which is then converted into wear volume. For detailed procedural and material considerations, refer to ASTM G99, [22].

In this study, both macro and micro-scale approaches are employed to model the pin-on-disc system using the Finite Element Method (FEM)—previous research by Salunkhe et al., [23], C. Curreli et al., [24], and Krishnamurthy et al., [25], have predominantly applied Archard's model for wear prediction in pin-on-disc setups. However, due to the model's miniature scale, the asperity-level approach has not been extensively explored in this context. Consequently, this study evaluates both modeling approaches using FEM and compares their outcomes to assess wear prediction performance.

Modelling methodology

To efficiently model wear at the microscale, a sub-modeling technique based on Saint-Venant's principle, [26] Is employed. This principle asserts that the stress field away

from the boundaries of a localized area remains relatively unchanged. In this approach, a global model is first created, then sectioned at boundaries away from the region of interest to form a smaller sub-model. The displacements at the cutting boundaries of the global model are transferred to the corresponding boundaries of the sub-model.

The flow chart for the wear modeling methodology is illustrated in Fig. 1. FEM pin-on-ring model is constructed to evaluate wear rates using either Archard's theory or single asperity modeling. In the Archard approach, the pin and ring surfaces are treated as flat and smooth, with contact pressure being evaluated accordingly. Conversely, the pin is modeled with surface roughness in the single asperity approach while the ring remains smooth and rigid. Here, sub-models are used to assess the contact stress of individual asperities. Using the Birth and Death element feature, a failure criterion is then applied to identify yielded elements removed from the model. The commercial FE application is utilized to build and solve the FEM models. Each step of this process is detailed in the following sections.

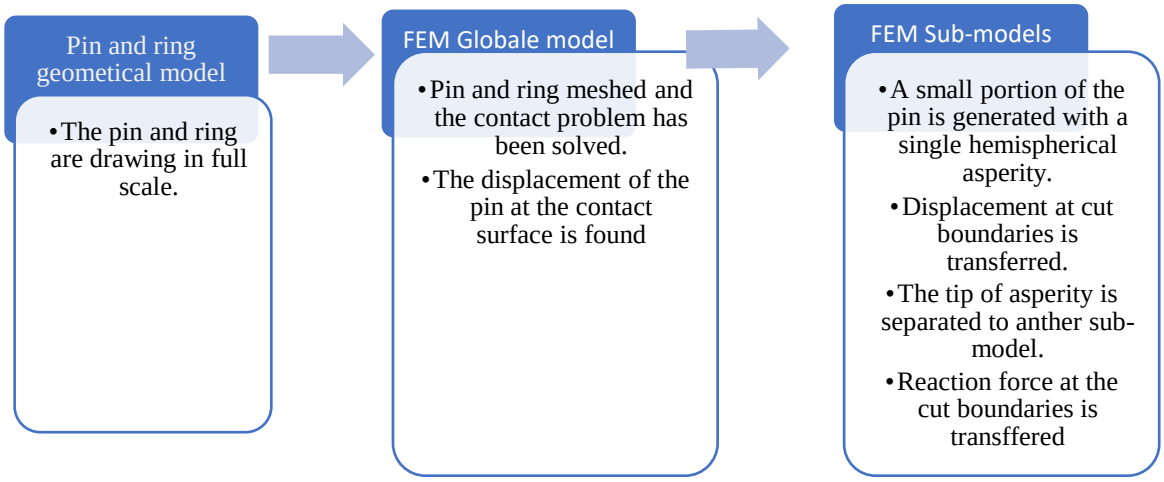

Fig. 1 Flow chart of wear rate evaluation methodology.

Global model

The global model, detailed in Fig. 2-a, is designed to compute pin wear height using Archard's theory and assess pin displacement under normal load, which is then incorporated into the sub-models. In this model, the pin is considered deformable and soft, while the ring is rigid, with both surfaces assumed to be smooth. The pin is discretized using linear solid elements (SOLID186), extending in the axis direction as illustrated in Fig. 2-b, whereas the ring is represented by a single surface element (SURF55). A contact/target technique, [27]. It simulates the frictional contact between the pin and ring, with a friction coefficient 0.2. The Augmented Lagrange formulation addresses the contact problem, and the target projected detection method is used to determine contact status. The contact stiffness is updated iteratively to reflect wear effects while other settings are maintained at their default values. Each simulation is conducted in two phases: the first determines contact pressure and sliding distance, which are then used in the ARCHARD module to calculate wear height and update

surface element displacement; the second phase runs until the pin displacement due to normal loads is ascertained.

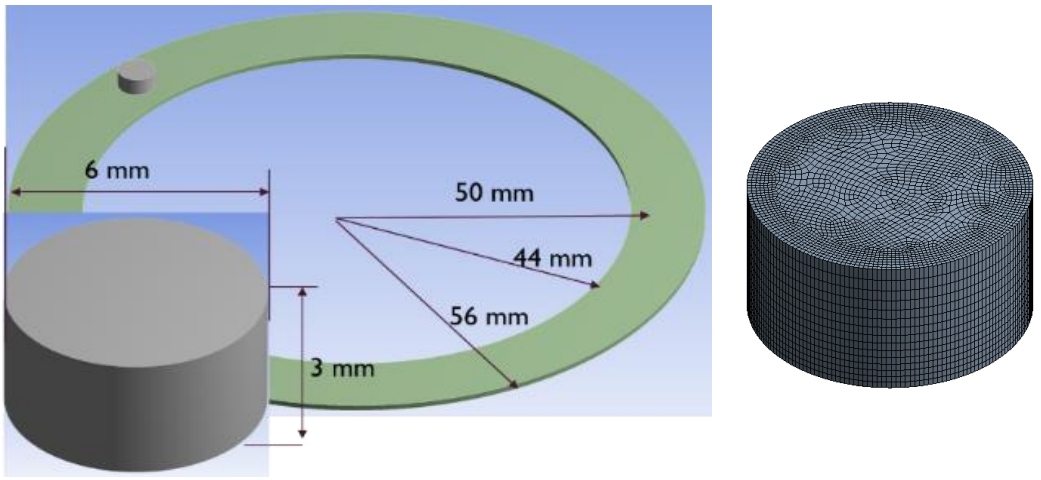

(a) (b)

Fig. 2 Pin on the ring, (a) model dimensions, (b) Pin FE model.

Boundary condition

To accurately simulate the pin-on-ring apparatus, the model incorporates three boundary conditions: a cylindrical boundary that fixes the pin in all directions except along the vertical axis, allowing movement solely in the vertical direction; a revolute joint between the ring and the global ground, enabling the ring to rotate around the vertical axis while remaining stationary in other directions; and a normal load applied to the top surface of the pin to replicate the pressing force typical of the pin-on-ring system.

Solution time steps and solver selection

In the first stage of the simulation, only the normal load is applied, with this phase lasting one second. Each wear prediction strategy has a specified time frame for subsequent steps, detailed in the following sections. The Archard theory and asperity-level approach utilize an iterative implicit solver for the simulations, ensuring stability and accuracy in the analysis of wear progression over time.

Mesh adaption study

The accuracy of the contact problem in FEM analysis is highly dependent on the number of elements used in the mesh. To ensure accuracy, a mesh-independent study was conducted. As illustrated in Fig. 3**, the contact pressure varies with the mesh size, showing that the variation stabilizes after using 200,000 elements. Consequently, this mesh size is selected for all subsequent analyses to balance precision and computational efficiency.**

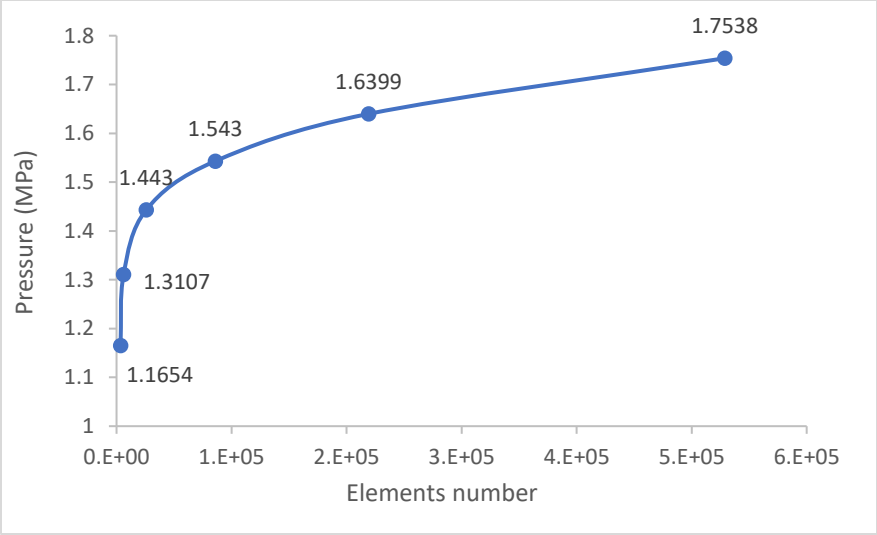

Fig. 3 Mesh adaptive curve based on maximum contact pressure relative to meshing elements number.

Global model validation

The accuracy of the global model is validated by comparing its results with theoretical findings from Hamilton et al., [28]. As illustrated in Fig. 4, the normal stress distribution exhibits asymmetry along the z-axis, with tensile stress observed at the trailing edge and compressive stress at the leading edge. This distribution aligns with Hamilton's results, where the maximum compressive stress location shifts in the direction of sliding due to the influence of friction. This comparison confirms that the model accurately represents the expected stress behavior.

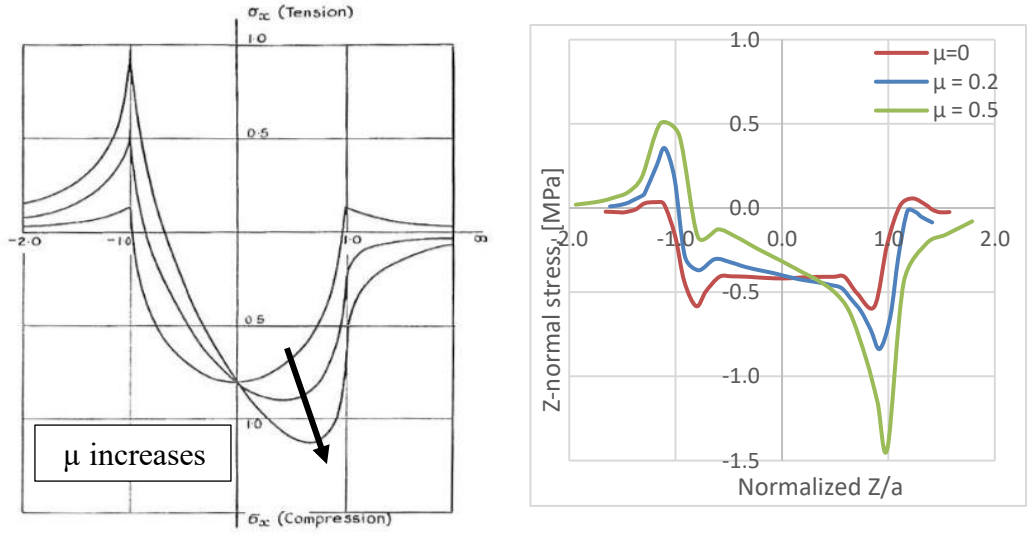

(a) **(b)**

Fig. 4 Normal stress over a pin diameter on contact surface for different friction coefficient (μ) comparison between (a) Hamilton et al. model, [28], and (b) present model.

Archard-based model

This approach predicts wear using a theoretical model to estimate adhesive wear volume. The Archard model for adhesive wear [8] It is a well-established method that correlates wear volume VT with the normal load (P), material hardness (H), and sliding distance (S). The equation defines the model:

$$V_T = K \frac{P}{H} S \qquad (1)$$

K is the dimensionless wear coefficient, representing the number of contacted asperities that produce adhesive wear, and is determined experimentally for a specific surface pair. The global model, as described in Section 3, is modified to compute wear volume using the Archard model integrated into the solver platform's material library to implement this equation. The model's mesh is refined, and a snippet command is added to activate Archard's module. The pin used in the simulation is made from Aluminum 7075-0, with properties listed in Table 2, and the deformation is considered elastic.

Time step criteria

An accelerated technique is employed to efficiently handle the computational demands in wear simulations. The current model achieves this by scaling the Archard equation with a significantly high sliding speed, such as 15,000 mm/s. This acceleration allows the simulation to finish in 2 seconds. This approach is similar to the techniques used in previous studies [24, 29]. The finite element model is solved using a workstation equipped with dual processors, 24 nodes, and a 3.5 GHz clock speed, with an average solving time of approximately two hours.

Archard-based Model validation

The Archard-based wear model is validated by comparing its results with experimental findings under similar conditions. An experiment by the authors, [23] investigated the wear characteristics of a pin made from aluminum alloy 7075 against an AISI 1060 steel ring using a pin-on-disc apparatus. In this setup, the disc was rotated at 200 rpm, and the pin was subjected to a normal load of 30 N, with the disc rotating until a sliding distance of 2000 meters was achieved. Fig 5 presents the wear height as a function of sliding distance, demonstrating good agreement between the experimental results and the model predictions. A comparison of wear parameters from the experiment with those obtained from the model shown in Table 1 Reveals a relative error in wear rate of less than 4 %. This close agreement confirms that the model is accurate and reliable for further analysis.

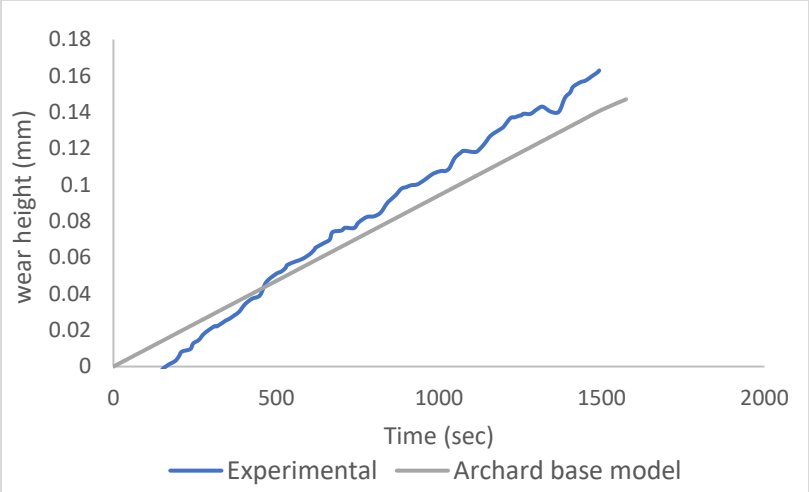

Fig 5 Wear height after traveling 3000 m as Salunkhe et al., [23], finding and the Archard-based model.

Table 1 Wear characteristics comparison between experiment finding and present model.

	Experimental	Archard model	Diff.
Sliding distance(m)	3000	3000	---
Wear coefficient (mm3/Nm)	4.42E-05	4.42E-05	---
Weight loss (g)	0.01126	0.01089	3.28%
Volume loss (mm3)	4.1094	3.9749	3.28%
Wear weight rate (mg/m)	0.00375	0.0036	3.19%
Wear rate (mm3/m)	0.0013	0.0013	3.28%
Wear height (mm)	0.1629	0.141	-13.31%

Sub-models (Asperity and tip models)

Simulating wear with practical accuracy necessitates a very high mesh density, especially at the asperity tip. A sub-modeling technique is utilized to address this, creating two distinct sub-models. The first, known as the asperity model, involves detaching a small section from the pin bottom and adding a hemispherical asperity with a radius of curvature (r_s) to the free surface of this section, as illustrated in Fig. 6. Due to geometrical symmetry about the vertical plane, only half of the asperity is considered, as shown in Fig. 7-a, with the geometry depicted in Fig. 7-b. The asperity's radius of curvature is set to 10 times the pin surface roughness (R_a), and its peak height is 10 % of Ra, [13, 30]. In the present model, the pin surface roughness is 0.123µm, adhering to the G88 standard for pin-on-disc testing, [22].The asperity shape is assumed to be a hemisphere with a contact radius of curvature, following the GW model, [31].The asperity model is discretized with a fine mesh to capture detailed interactions.

Additionally, a second sub-model termed the tip model, is created from the tip of the asperity, as depicted in Fig. 8, to facilitate a more efficient simulation process. The

finite element gridding for both models is shown in Fig. 9. For the analysis, these two sub-models are combined into a single model known as the asperity-level model, allowing for comprehensive wear simulation at the asperity scale. For full stick condition, a bounded contact is established between the asperity tip and a sub-ring for both sub-models.

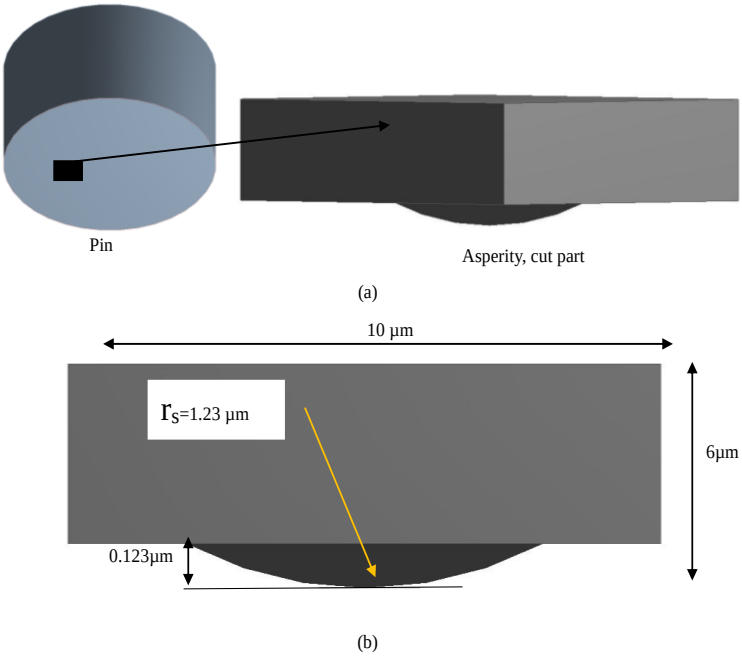

Fig. 6 Asperity model generation, (a) pin cutting part that contains single asperity and (b) the model dimensions.

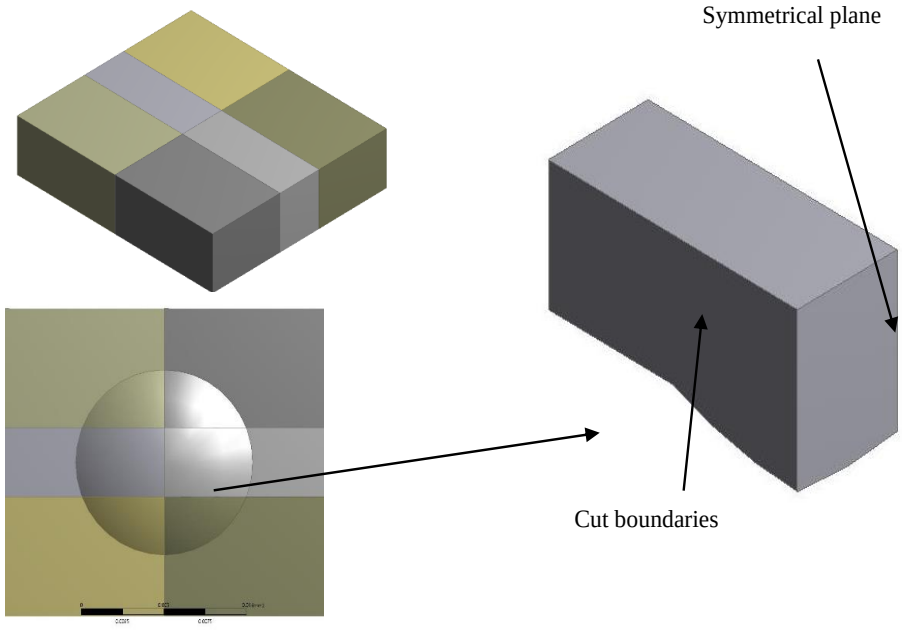

Fig. 7 Asperity geometry reduction utilized symmetry, (a) Asperity geometry partitioning, and (b) asperity model.

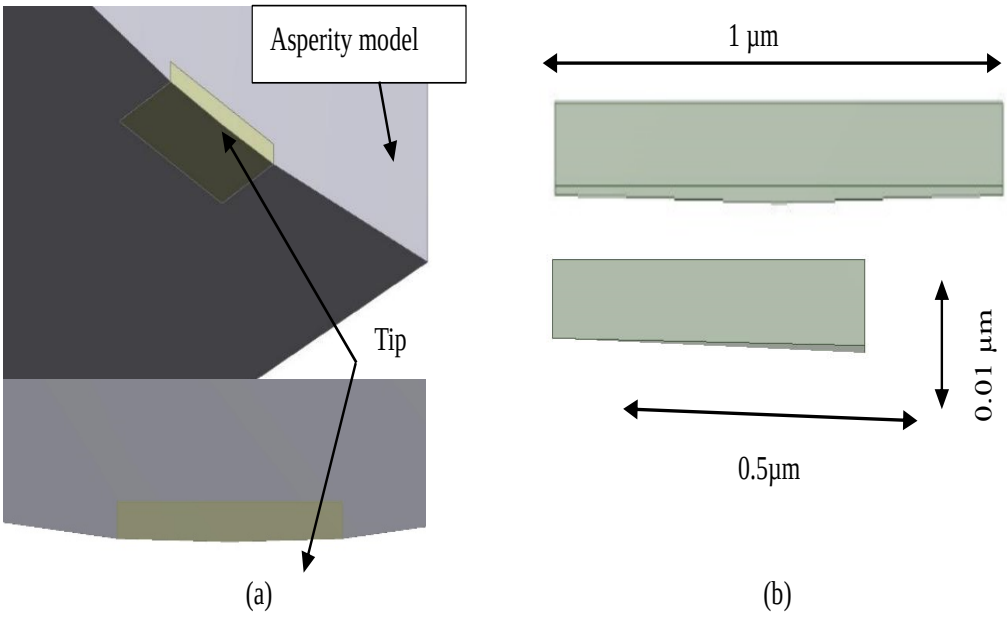

Fig. 8 Tip model, (a) Asperity tip geometry, (b) the model dimension.

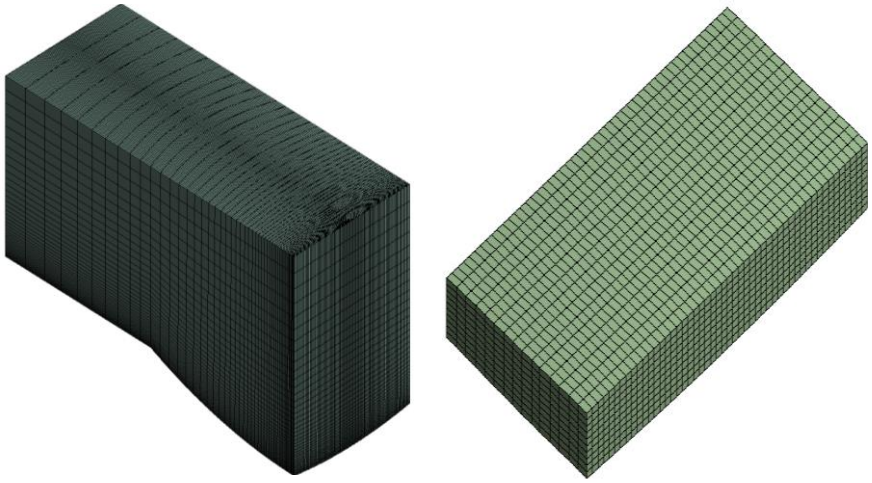

(a) **(b)**

Fig. 9 Microscale FE models, (a) Asperity model, (b) Tip model.

Haibo Zhang and Izhak Etsion, [17]. A comparable study was conducted on a larger scale and suggested that for accurate simulation of plastic deformation, the minimum mesh element size should be 0.05 times the sphere radius (r). Based on this recommendation, a mesh size of 5×10^{-5} mm is used for the asperity model. For the tip model, the mesh is adaptively refined, with the mesh size varying between 2.5 and 5 times the element number, as illustrated in Fig. 10 **This approach ensures precise modeling of the wear phenomena at the asperity and tip levels.**

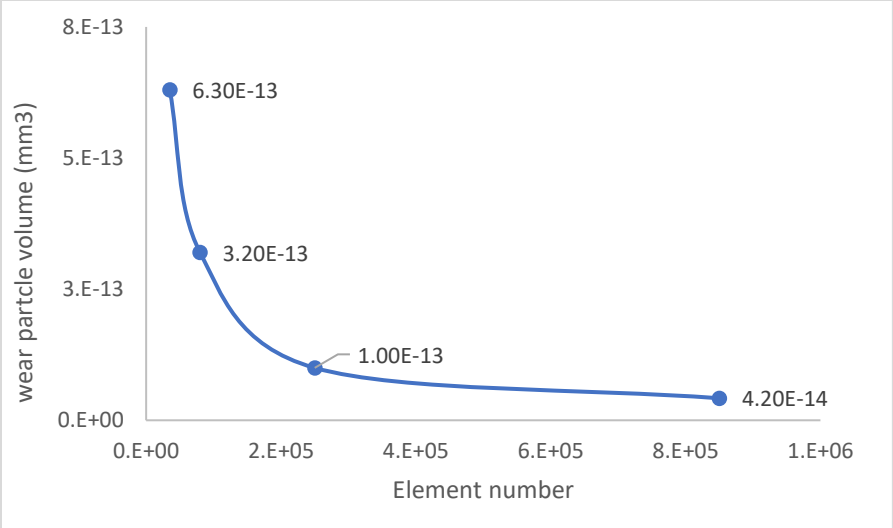

Fig. 10 Mesh adaptive curve for the tip model based on wear particle volume relative to the number of elements.

Boundary conditions (B. Cs)

The displacement constraints from the cut boundaries of the global model are transferred to the corresponding surfaces of the asperity model, as illustrated in Fig. 11. In this setup, the reaction force computed from the asperity model is applied to the top surface of the tip model, as depicted in Fig. 12. The sub-ring in the asperity model is fixed, while in the tip model, it is connected to the ground with a revolute joint, permitting rotation around the vertical axis. A tangential displacement is introduced using a small angular step of 1×10^{-7} radians.

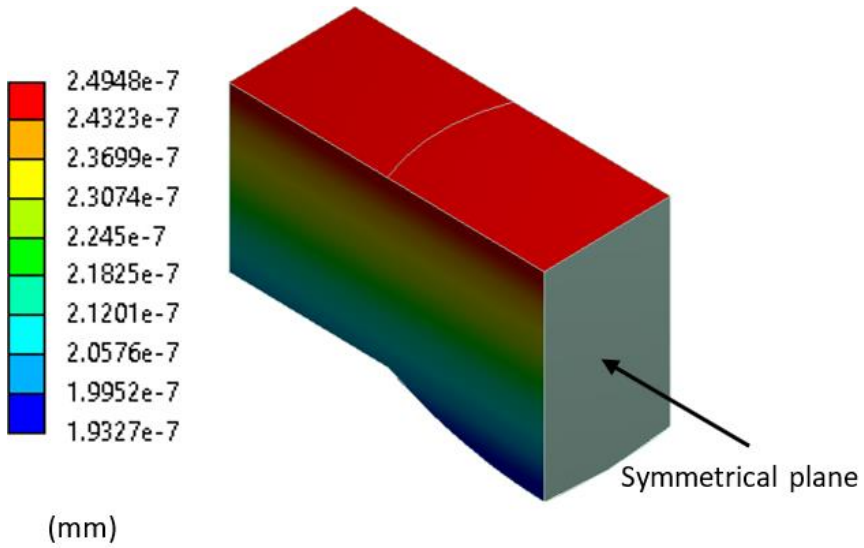

Fig. 11 Displacement transferred from the global to the asperity model.

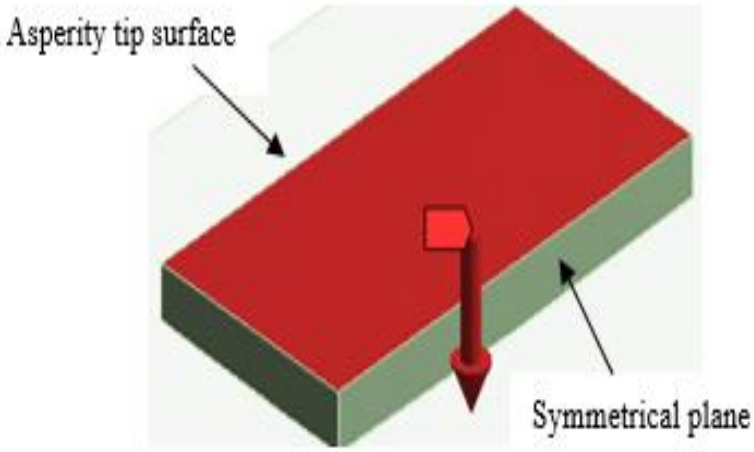

Fig. 12 Normal force transferred from the asperity model to the tip model.

Solving process

The solving process begins with the global model to establish contact between the pin and the ring to determine the wear particle generated from the asperity's tip. Once this contact is established, the asperity model is executed to determine the corresponding displacement of the asperity. Subsequently, the tip model is used, applying the transferred normal reaction force from the asperity model to simulate crack propagation over the contacted patch and the formulation of a wear particle. The global and asperity models each use four-time steps of 0.25 seconds. For the tip model, time marching is done with a 0.05-second step during the initial period of normal load application and a 0.1-second step for the remaining simulation period. Each time step is further divided into smaller sub-steps based on deformation rates using the auto-stepping method. The tip model is run until a complete crack form around the contact patch, with the wear particle represented by the remaining active elements in the contact patch. The FE models are solved on a workstation with dual CPUs and 24 nodes at 3.5 GHz, with an average solving time of two hours for the asperity-level model and six hours for the tip model, resulting in a total of 12-time steps: 4-6 steps in the first stage for normal load application and additional steps for crack initiation and propagation.

Fracture model

The formulation of wear particles requires a fracture criterion; the Johnson-Cook crack initiation theory is used as done, [16, 17, 19]. Assuming isothermal and quasistatic behavior, the plastic strain for crack initiated is stated in:

$$\varepsilon_p = C_1 + C_2 e(-C_3 \sigma_T) \qquad \textbf{(2)}$$

Where ε_p **is the plastic strain,** C_1, C_2 and C_3 **Are model coefficient depend on the material,** σ_T **is stress triaxiality that is defined as:**

$$\sigma_T = \frac{\sigma_D}{\sigma_q} \qquad \textbf{(3)}$$

Where σ_D is deviatoric or hydrostatic stress which is equal to:

$$\sigma_D = \frac{1}{3}\left(\sigma_x + \sigma_y + \sigma_z\right) \qquad \textbf{(4)}$$

and σ_q is the equivalent stress:

$$\sigma_q = \sqrt{(\sigma_1 - \sigma_2)^2 + (\sigma_2 - \sigma_3)^2 + (\sigma_3 - \sigma_1)^2} \qquad \textbf{(5)}$$

Where σ_1, σ_2 and σ_3 are the principal stresses

The model coefficients are found experimentally and thoroughly examined for aluminum alloy, [32, 33].

Table 3 depicts the coefficient values used in this study. A crack propagation criterion should be included to avoid solution diverging, [17], strain energy for crack propagation theory has been implemented to find the plastic strain where the material loading capacity diminished and failed. This energy is defined as, [21]:

$$SE = \int_{\varepsilon_p}^{\varepsilon_f} \sigma_y \varepsilon d\varepsilon \qquad \textbf{(6)}$$

Where SE is the strain energy, σ_y is material yield stress, $\varepsilon_f = 0.025$ is the plastic strain at fracture, for aluminum alloy, SE equal to 20 KJ/m^2, [21]. The stress triaxiality is evaluated at the beginning of each time step, and the fracture criterion is set, so any element with plastic strain exceeding this criterion will be deactivated.

Material modeling and properties

Aluminum 7075-0 is used for all models due to its favorable mechanical properties, which include high strength and good fatigue resistance. This alloy is widely recognized for its excellent performance under dynamic loading conditions, making it suitable for wear simulation studies. Its well-documented behavior under various loading scenarios ensures reliable and consistent model results. Additionally, using a standard material like Aluminum 7075-0 allows for comparison with existing experimental data and validation of the modeling approaches.

Table 2 Mechanical properties of untampered aluminum alloy-7075, [34].

Elastic modulus, E, MPa	**70710**
Yield strength, Y, MPa	**140**
Ultimate tensile strength, U, MPa	**280**
Tangent modulus, E_T, MPa	**17237,[35]**

Table 3 Johnson-cook model- coefficients, [32, 33].

C_1	**0.025**
C_2	**0.15**
C_3	**-1.5**

Wear volume estimation method

The pin surface roughness(R_a) and the standard deviation(σ) where the surface mean line lay on the nominal pin surface area $\sigma = 1.25R_a$ mm, [9]. The asperity density, λ (asperity/mm^2) and the asperity radius of curvature (r_s), which those parameters are related as shown in [36], by a surface roughness parameter(Γ) that is defined by:

$$\Gamma = \lambda \sigma r_s \qquad \textbf{(7)}$$

The total number of asperities of a given surface (*N*) is defined by:

$$N = \lambda A \qquad \textbf{(8),}$$

where A is the apparent contact area.

Assuming the surface roughness follows a normal Gaussian distribution, [13], with a probability function:

$$\Phi(z) = \frac{1}{\sigma\sqrt{2\pi}}\left(\frac{-(\mu - z)}{2\sigma^2}\right) \qquad \textbf{(9)}$$

where μ is the mean and equal to R_a, z is the asperity height coordinate, and the asperities are laid off the mean surface, so the contact asperities are above the mean line and have peak height more significant than the mean value;

Thus, the number of contact asperities could be defined as:

$$N_S = N \int_l^{\infty} \phi(z)dz \qquad \textbf{(10)}$$

Where *l* is the separation distance between the mean surface and rigid surface, and to evaluate it, the Kogut and Etsion model, [37], is implemented, the authors define the standard deviation of the asperities by σ_s and related to the contact surface standard deviation (σ) by:

$$\frac{\sigma}{\sigma_S} = \sqrt{1 - \frac{3.717 \times 10^{-4}}{\Gamma^2}} \qquad \textbf{(11)}$$

The separation between the rigid surface and the asperity mean surface is l_S as defined in [37], each length is normalized by σ_s , while herein, the difference between two mean surfaces, in dimensional form, is determined from:

$$l = \sigma_S \frac{1.5}{\sqrt{108\pi\Gamma}} + l_S \qquad \textbf{(12)}$$

The critical interference of the asperities for plastic inception is defined as:

$$\delta_c = \left(\frac{\pi \nu H}{2E}\right)^2 r_s \qquad \textbf{(13)}$$

Where H is the hardness factor, and it is related to Poisson's ratio (ε) by:

$$\nu = 0.454 + 0.41\varepsilon \qquad \textbf{(14)}$$

The plasticity index(ψ) is defined, [13], and determines the deformation mode, which is related to the material properties, surface parameters, and asperity's radius of curvature and is evaluated by:

$$\psi = \frac{2E}{\pi \nu H}\sqrt{\frac{\sigma_S}{r_S}} \qquad (15)$$

In this model, [37], inequality between plasticity index and separation distance is established based on the maximum available asperity height.

$$\psi > \sqrt{\frac{\delta / \delta_C}{3 - l_s / \sigma_S}} \qquad (16)$$

Where δ is asperity interference, from equations (11) to (16), the lower limit of integration of the equation (10) could be evaluated, thus the total wear volume due to all contacting asperities, V_T It is defined by:

$$V_T = N_c V_p \qquad (17)$$

Where V_p is single asperity wear volume, computed from the asperity-level model, the sliding distance, S, at the instance where the wear particle formulated, is defined as: where is single asperity wear volume, that is computed from the asperity model. The sliding distance, S, at the instance where the wear particle is formulated, is defined as:

$$S = \beta r_p + L_e \qquad (18)$$

Where β Is turning angle in radian, just before wear formulation, L_e is the wear particle length, finally, the wear rate, W_r , defined as:

$$W_r = \frac{V_T}{S} \qquad (19)$$

Asperity-level model validation

The surface roughness parameter, Γ Tank a value in the range of 0.05 to 0.04, [37, 38], and $\Gamma = 0.05$ is applied in the equation (7), so, $\lambda = 258098\ asperity / mm^2$, and the total number of asperities for the pin surface given by the equation (8), $N \approx 7.5 \times 10^6$ Asperities. The material properties depicted in the asperity radius of curvature and surface parameters that are defined in section 0 have to apply equations (9) to (17). These are used to find the total wear volume of the pin for normal load = 30 N. The simulation depicted that wear particle is formed at the angular displacement, β , is 1e-6 rad, and its length is L_e=3e-4 mm; then, the sliding distance is estimated by the equation (18), S = 3.03×10^{-4} mm, and the wear volume per asperity is V_s = 9.9 × 10^{-9} mm^3, (model outcome); then, the total wear rate is evaluated from equation (19) W_r = 3.3 × 10^{-2} mm^3/m and the dimensional wear coefficient (K) is K = 1.3 × 10^{-3} mm^3/Nm. The model finding compared with the experiment finding of Salunkhe, [23], as shown in Table 4

Table 4 Results comparison between experiment and present model

	Wear rate (mm^3/m)	Wear coefficient, K_D (mm^3/Nm)
Experiment	**1.36×10^{-3}**	**4.41×10^{-5}**
Asperity model	**3.3×10^{-2}**	**1.3×10^{-3}**

The discrepancy between the asperity-level model and the experiment is because the surface characteristics are approximately defined, whereas the actual values are not available, and a correlation factor, Cf, is used, which is defined as $Cf = \frac{\text{model wear rate}}{\text{experimental wear rate}} = 0.042$**, and the further evaluated wear rate will be multiplied by it. For the 30 N load case, the correlated wear coefficient, Cf, is 4.77×10-5 (mm3/Nm) with an 8.2 % relative error for the predicted wear rate.**

RESULTS AND DISCUSSIONS

Archard-based model

The wear rate variation with load and sliding speed is demonstrated in Fig. 13 and Fig. 14. The wear rate exhibits a linear relationship with load, consistent with Archard's theory, [8], for light to moderate wear. In contrast, the wear rate remains independent of sliding speed, aligning with the prediction of Archard's model, which indicates that sliding speed does not significantly influence wear rate in the studied conditions.

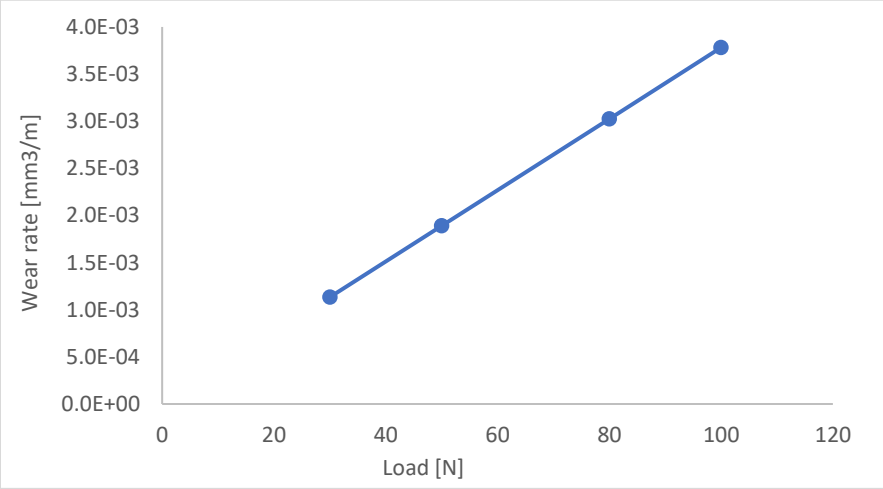

Fig. 13 Wear rate variation with normal load, as depicted from the Archard-based model.

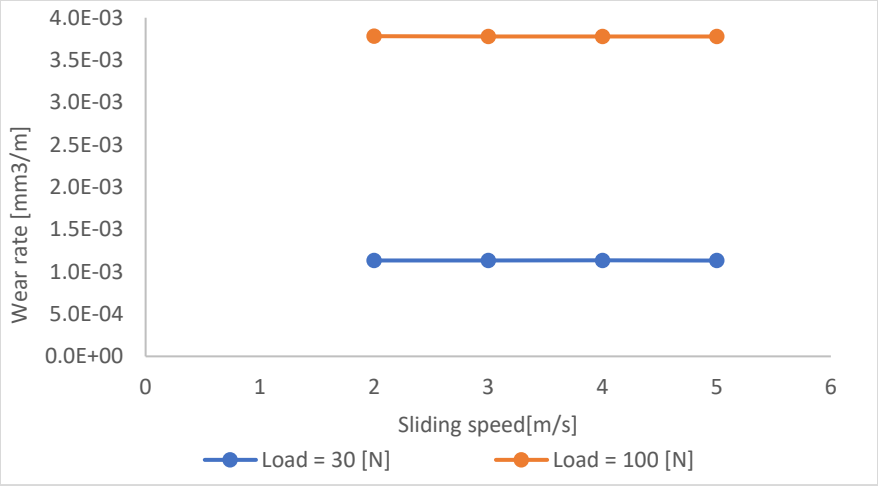

Fig. 14 The wear rate for different sliding speeds, as evaluated from the Archard-based model.

The pin's normal stress distribution over the pin's surface before and after wear under a 30 N load is illustrated in Fig. 15 - a and b, respectively. The results show that the compressive normal stress at the trailing edge, just before the circumference, decreases by 50 % due to wear. In comparison, the central region experiences a 25 % increase in compressive stress, and the leading edge sees a 20 % increase. This stress redistribution is attributed to the frictional forces causing the leading edge to dig into the ring while the trailing edge experiences reduced contact. In contrast, V.G. Salunkhe et al., [23] developed a similar model, shown in Fig. 13 c and d, where the circumferential normal stress decreases only slightly due to wear, with no significant directional effect on stress variation. This difference is likely because Salunkhe's model did not account for the actual rotational movement of the ring, which plays a crucial role in stress distribution in your analysis. The wear height distribution is shown in Fig. 16, as depicted, the leading-edge wear height is higher than the trailing edge due to higher compression stress.

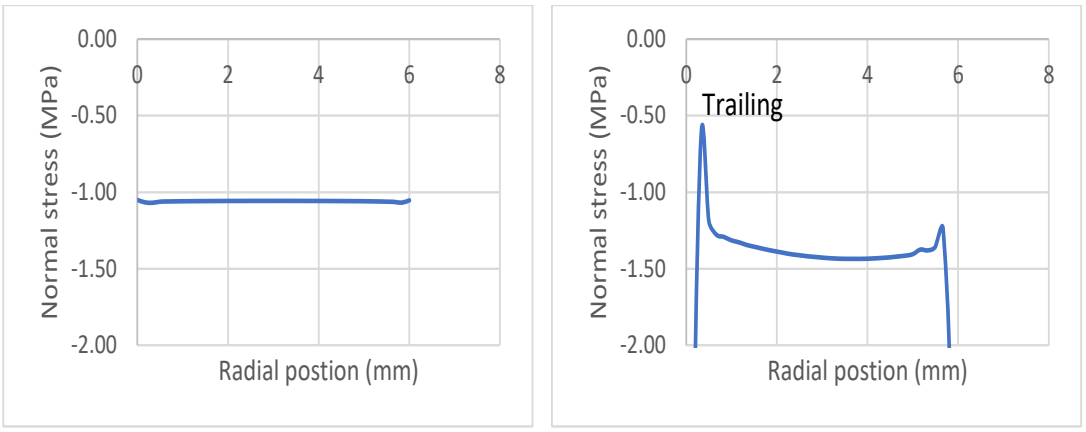

(a) (b)

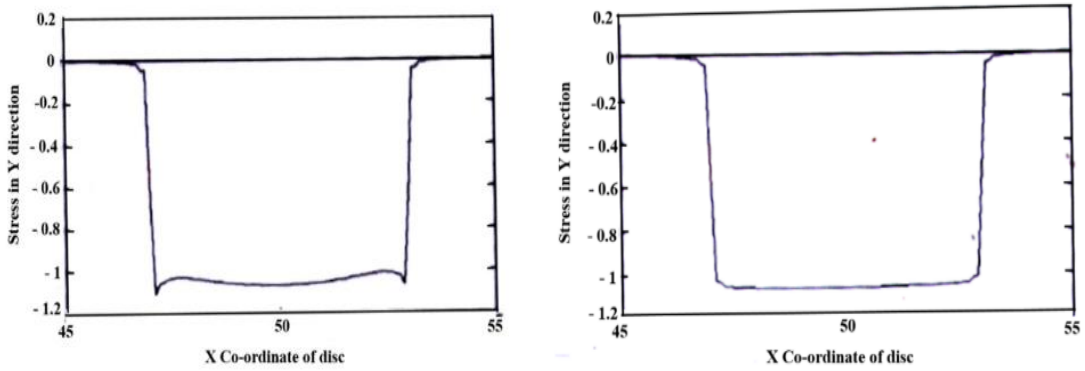

(c) (d)

Fig. 15 Normal stress variation over pin cord due to wear, under 30 N, Archard-based model finding depicted in (a) and (b), while V.G. Salunkhe et al., [23], depicted in (c) and (d).

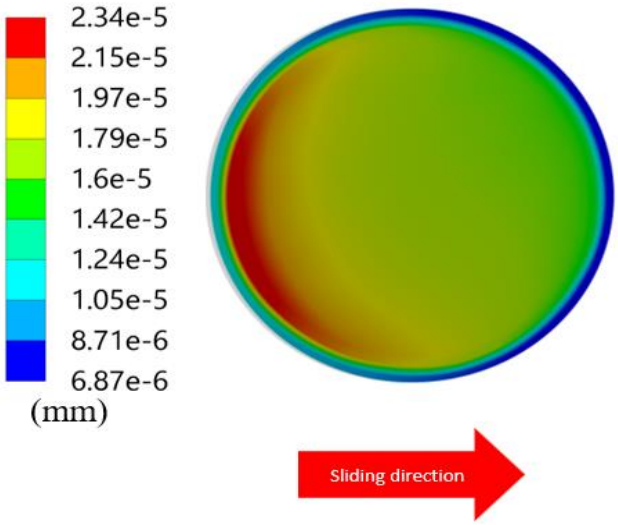

Fig. 16 Wear height distribution for 30 N normal load and 30 m sliding distance.

The wear particle is formed after a tip crack extends around the contact zone, with the volume of the remaining elements in contact representing the wear volume for a single asperity. The tip crack is highlighted. Fig. 17-a as a narrow red zone. As this crack propagates from the leading edge to the trailing edge, a wear particle is created, as shown in Fig. 17 - b under a 30 N load. For other loads, the corresponding wear particles are depicted in Fig. 18, demonstrating that both the length and volume of the wear particles increase as the load increases

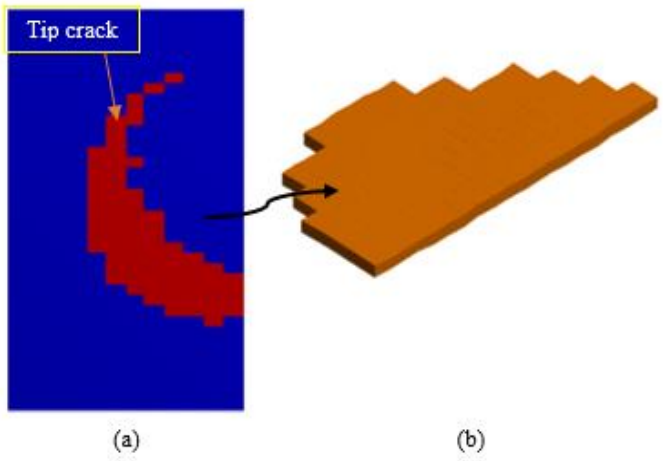

Fig. 17 Estimated asperity tip failure at the end of the solution, for 30 N and 1e-6 rad, (a) asperity tip crack, (b) formulated particle.

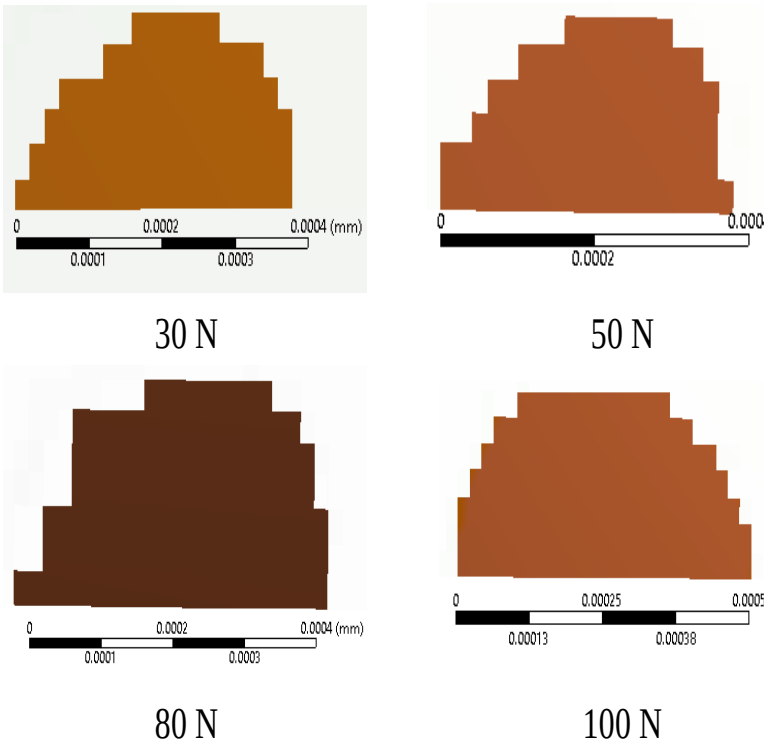

Fig. 18 The wear particle shapes for different normal loads, Top view.

The wear rate, as shown in Fig. 19, demonstrates a non-linear variation with the load, aligning with the findings of J. Archard and W. Hirst, [39]. This states that at high loads, the linear proportionality of wear to load may no longer hold, and instead, an exponential relationship may develop. The wear coefficient, estimated by the asperity-level model and multiplied by Cf, is shown in Fig. 20. The variation of the wear coefficient with contact pressure (p) demonstrates a decrease as (p) increases (Fig. 20 - b), which contrasts with the findings of Halling, [4], where the wear coefficient is independent of contact pressure until it reaches H/3, which increases exponentially.

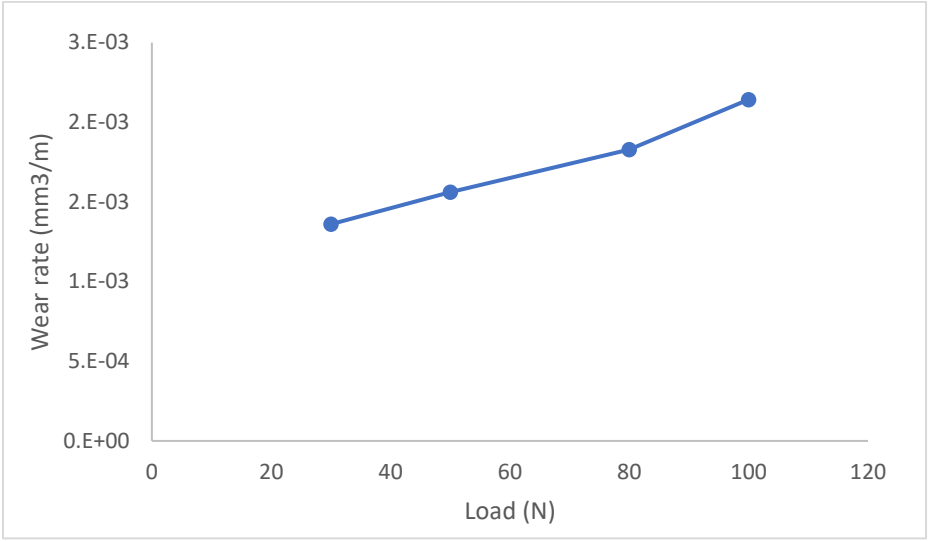

Fig. 19 Wear rate against a load that is evaluated from the asperity-level model.

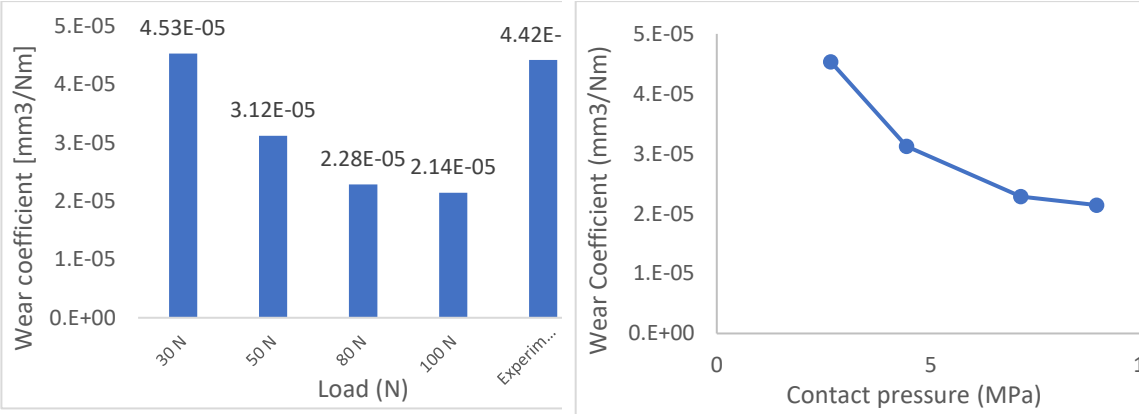

(a) **(b)**

Fig. 20 Wear coefficient variation, determined from asperity-level model (a) with load, (b) with contact pressure.

L. Feroz Ali et al., [40], The effect of matrix composition coating on wear rate was studied, but uncoated samples were tested as a baseline for comparison with the findings of current models. Fig. 21 shows the wear rate in mg/mm for two models. Although the Archard model overestimates the wear rate at higher loads, both models exhibit similar behavior to the experimental results.

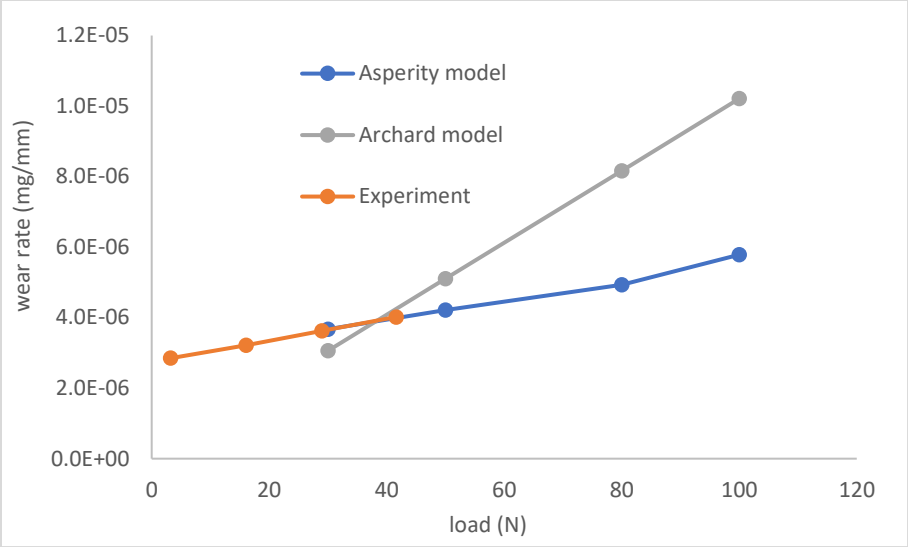

Fig. 21 Results of wear rate in mg/mm were compared with the experimental results, [40].

The coefficient of friction, COF, is estimated as $\frac{\text{tangential force}}{\text{normal load}}$**, and Brizmer et.al., [41], express the COF as a function of relative load that is defined by:**

$$Rl = \frac{F_n}{F_c} \qquad \textbf{(20)}$$

Where F_n **is the normal load,** F_c **is the critical load at sliding inception and defied by:**

$$F_c = \frac{\pi^3}{6}\bar{\nu} * \sigma_y * cv^3 * (3*(1-\nu^2)*\sigma_y / E)^2 \qquad \textbf{(21)}$$

Where $\bar{\nu}$ **is function on Poisson's ratio and defined by:** $\bar{\nu} = 8.88\nu - 10.13(\nu^2 + 0.089)$ **.**

Fig. 22 depicts the static coefficient of friction (COF) compared with Brizmer's equation, [41]. They show that the model's COF is higher than the suggested value. The authors proposed that the static COF reaches a constant value after full plastic deformation. However, in the present study, the COF decreases as plastic deformation increases, even in the fully plastic zone. This discrepancy may be attributed to differences in the material model's parameters, particularly the tangent modulus. Although both studies use a bilinear material model, Brizmer et al. set the tangent-to-elastic modulus ratio to 2 %, while in the current study, it is set to 24 %. These differences highlight that the static friction coefficient strongly depends on the material plastic behavior.

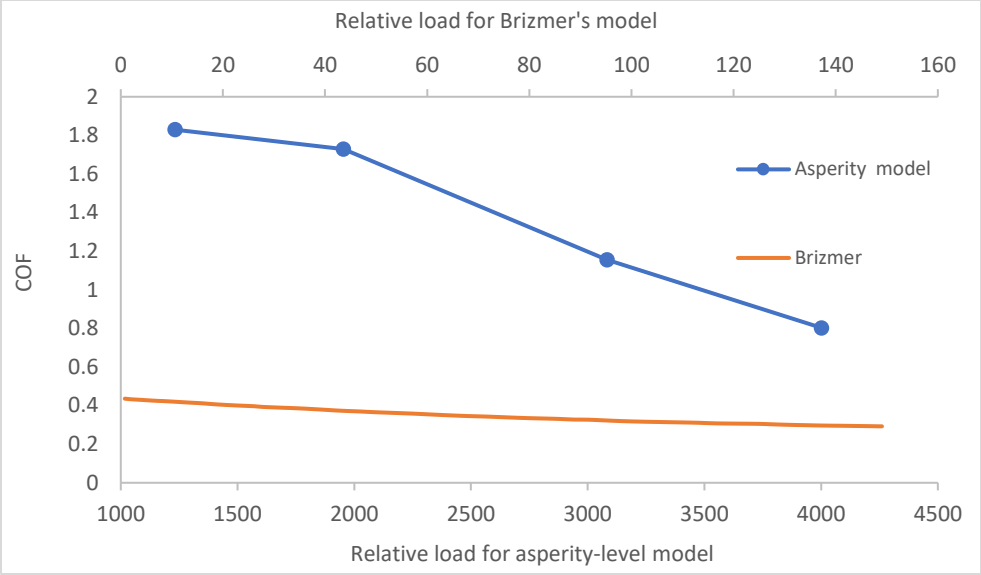

Fig. 22 Static coefficient of friction, compared with Brizmer equation, [19].

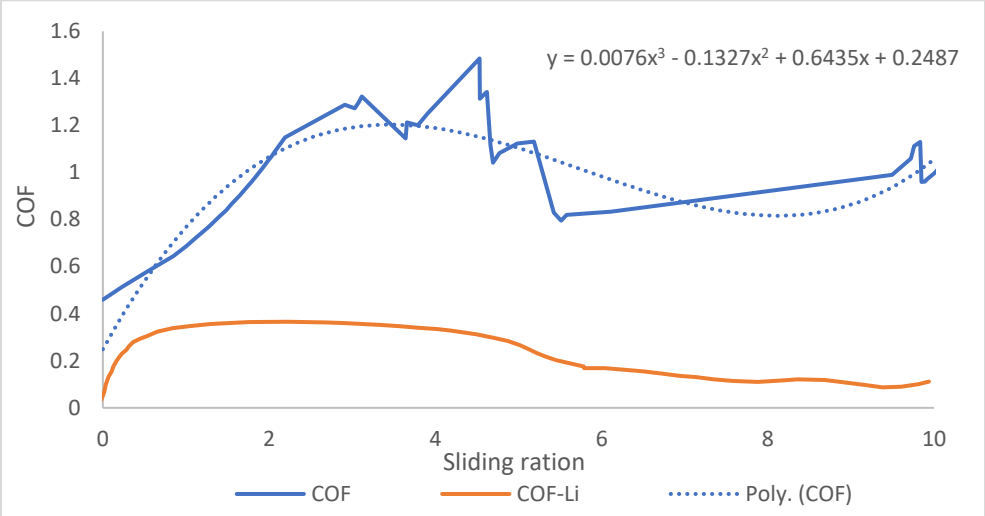

Fig. 23 COF changes till sliding occurs, and it is a static friction coefficient.

The coefficient of friction, COF, changes with the sliding distance until complete slipping from the contact surface that is shown in Fig. 23 and compared with, [19], model finding: the ratio of the slip distance to the initial interference due to normal load only, $\delta_R = \frac{u}{\delta_i}$, is used in the x-axis. As depicted in the figure, the friction coefficient increases gradually with δ_R Till reach the maximum at the slip displacement equal to four times the initial interference $\delta_R = 4.5$. It decreases with further slippage to reach a constant value equal to 0.8 at $\delta_R = 5.6$ and slightly increased to 1 at sliding inception, which is defined as a static friction coefficient;

similar behavior is found, [19]. However, a higher slope is found at the beginning of slipping. It reaches a maximum value of 0.3 at 2.5 relative sliding and 0.16 at 5.6 relative distance, which further decreases to 0.1 at the sliding inception. The static COF evaluated from the Li et al. model is 30 % lower than the present model; this mismatching finding may be because of the geometrical scale difference between both models; in Li's model, the sphere radius is taken in the range from 5 to 50 mm while in the current study, the asperity level is used, r_s = 0.1 µm, subsequently, the relative load, Rl , in the current model, it is in the range of (1000-4000) while, for Li's model, it is in the range of 1 to 150, so the deformation is very high in the present model, and so is the COF. The approximated function of COF is shown as a 3rd-order polynomial function.

The coefficient of friction (COF) changes with the sliding distance until it completely slips from the contact surface. Fig. 22, and is compared with the findings, [19]. The x-axis represents the ratio of the slip distance to the initial interference caused by the normal load alone. The figure demonstrates that the friction coefficient gradually increases with the slip ratio, reaching a maximum when the slip displacement equals four times the initial interference. Afterward, it decreases with further slippage, stabilizing at a constant value of 0.8 and slightly increasing to 1 at the point of sliding inception, which is defined as the static friction coefficient. A similar behavior is observed, [19], but with a steeper initial slope, reaching a maximum COF of 0.3 at 2.5 relative sliding and decreasing to 0.16 at 5.6 relative distance, eventually dropping to 0.1 at sliding inception. The static COF calculated from Li et al. model is 30 % lower than the present model, likely due to geometric scale differences. In Li model, the sphere radius ranges from 5 to 50 mm, while in the current study, the asperity level is used with r_s = 0.1 µm. Consequently, the relative load in the current model is between 1000 and 4000, whereas in Li model, it ranges from 1 to 150, resulting in much higher deformation and, thus, a higher COF in the present model. The approximated function of COF is a 3rd-order polynomial.

Models comparison

The model results demonstrated wear volume as a function of normal load, with the Archard-based model showing a linear relationship between wear rate and normal load, independent of sliding speed. In contrast, the asperity model exhibited non-linear behavior. As shown in Fig. 24, the Archard-based model predicted higher wear increments than the asperity model. Regarding applicability, the Archard-based model offers an easy-to-use method suitable for more complex modeling problems. In contrast, the asperity model provides deeper insight into the influence of surface parameters on adhesion wear. Accurate wear predictions can be made with the asperity model if surface parameters are known, but its scale makes it challenging to implement for complex contact systems. Additionally, the Archard-based model can be applied to lubricant contact scenarios, whereas the asperity model is limited to dry surface conditions due to the contact theories it employs. Regarding computational efficiency, evaluating wear volume using the asperity-level model took eight hours for a single case, while the Archard model required only two hours for a similar case.

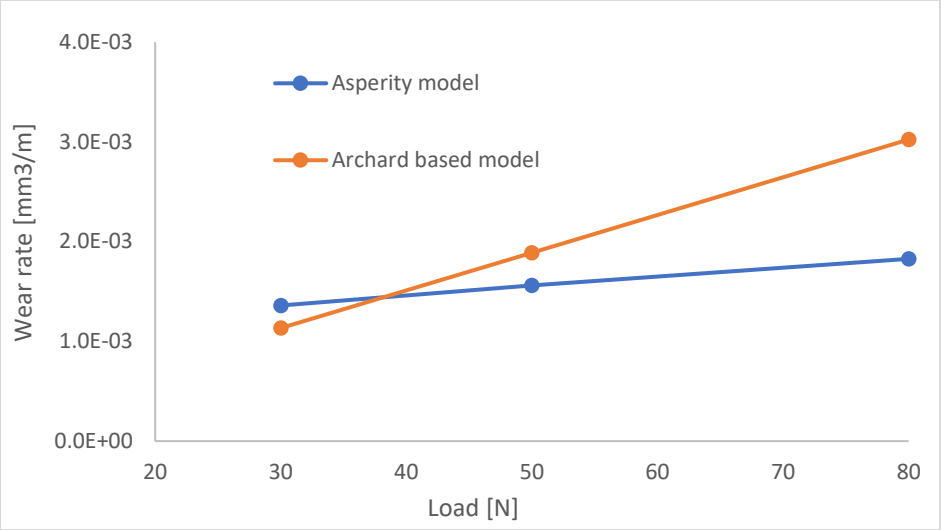

Fig. 24 Wear rate for different applied loads and 40 mm/s sliding speed, as evaluated from present models.

CONCLUSIONS

This study explores adhesive wear prediction using finite element modeling with two approaches: an Archard-based model and an asperity-level model. The Archard model, which shows a linear relationship between wear rate and load, is practical for complex systems but requires empirical calibration. In contrast, the asperity-level model offers detailed insights into the non-linear relationship between surface roughness and wear, though its complexity limits its application to simpler systems. It also tends to overestimate static friction coefficients. While the Archard model is more versatile, particularly for lubricated environments, future research should focus on improving the accuracy of surface parameters in the asperity model and expanding its applicability to more complex and lubricated systems.

REFERENCES

1. Burwell Jr and J. T., Survey of possible wear mechanisms. Wear, 1957. 1(2): p. 119-141.

2. Mulvihill, D.M., et al., An elastic–plastic asperity interaction model for sliding friction. Tribology International, 2011. 44(12): p. 1679-1694.

3. Yastrebov, V.A., G. Anciaux, and J.-F. Molinari, On the accurate computation of the true contact-area in mechanical contact of random rough surfaces. Tribology International, 2017. 114: p. 161-171.

4. Halling, J., Principles of tribology. 1978: Macmillan International Higher Education.

5. Johnson, K.L.K.e.n.d.a.l.l.K.R., A. N. D. , Surface energy and the contact of elastic solids. Proceedings of the Royal Society of London. A. Mathematical and Physical Sciences, 1971. 324(1558): p. 301-313.

6. Prokopovich, P. and V. Starov, Adhesion models: from single to multiple asperity contacts. Adv Colloid Interface Sci, 2011. 168(1-2): p. 210-22.

7. Brizmer, V., I. Etsion, and Y. Kligerman, A Model for Junction Growth of a Spherical Contact. 2007.

8. Archard, J.F., Contact and Rubbing of Flat Surfaces. Journal of Applied Physics, 1953. 24(8): p. 981-988.
9. Brushan, B., Modern Tribology Handbook,. 2001, CRC Press LLC.
10. Zum Gahr, K.-H., Microstructure and wear of materials. Vol. 10. 1987: Elsevier.
11. Zhang, H., R. Goltsberg, and I. Etsion, Modeling Adhesive Wear in Asperity and Rough Surface Contacts: A Review. Materials (Basel), 2022. 15(19).
12. Rabinowicz, E., The effect of size on the looseness of wear fragments. Wear, 1958. 2(1): p. 4-8.
13. Greenwood, J.A., Williamson, J. B. P., Contact of nominally flat surfaces. Proceedings of the Royal Society of London. Series A. Mathematical and Physical Sciences, 1966. 295(1442): p. 300-319.
14. Cohen, D., Y. Kligerman, and I. Etsion, A model for contact and static friction of nominally flat rough surfaces under full stick contact condition. 2008.
15. Hu, G.-D., et al., Adaptive finite element analysis of fractal interfaces in contact problems. Computer methods in applied mechanics and engineering, 2000. 182(1-2): p. 17-37.
16. Zhang, H. and I. Etsion, An advanced efficient model for adhesive wear in elastic—plastic spherical contact. Friction, 2022. 10(8): p. 1276-1284.
17. Zhang, H. and I. Etsion, Evolution of adhesive wear and friction in elastic-plastic spherical contact. Wear, 2021. 478-479.
18. Molinari, J.-F., et al., Adhesive wear mechanisms uncovered by atomistic simulations. Friction, 2018. 6(3): p. 245-259.
19. Li, M., G. Xiang, and R. Goltsberg, Efficient Sub-Modeling for Adhesive Wear in Elastic–Plastic Spherical Contacts. Lubricants, 2023. 11(5).
20. Lawn, B. and R. Wilshaw, Indentation fracture: principles and applications. Journal of materials science, 1975. 10: p. 1049-1081.
21. Hillerborg, A., M. Modéer, and P.E. Petersson, Analysis of crack formation and crack growth in concrete by means of fracture mechanics and finite elements. Cement and concrete research, 1976. 6(6): p. 773-781.
22. Methods, A.T., Standard Test Method for Wear Testing with a Pin-on-Disk Apparatus1. Wear, 2011. 5: p. 1-5.
23. Salunkhe, V.G., et al., Simulation and experimental studies on sliding wear of aluminum alloy under dry condition using asymmetric contact models. 2019.
24. Curreli, C., L. Mattei, and F. Di Puccio. Finite element simulations of pin-on-disc wear tests using submodeling. in Proceedings of the XXIII conference of the Italian association of theoretical and applied mechanics. 2017. GECHI EDIZIONI.
25. Krishnamurthy, N., et al., A Study of Parameters Affecting Wear Resistance of Alumina and Yttria Stabilized Zirconia Composite Coatings on Al-6061 Substrate. ISRN Ceramics, 2012. 2012: p. 1-13.
26. Mises, R.v., On Saint Venant's principle. Bulletin of the American Mathematical Society, 1945. 51: p. 555-562.
27. ANSYS, I., ANSYS Mechanical APDL Contact Technology Guide. 2017: U.S.A.
28. Hamilton, G.M. and L.E. Goodman, The stress field created by a circular sliding contact. Journal of Applied Mechanics, 1966. 33(2): p. 371-376.

29. Torres Pérez, A., et al., A model of friction for a pin-on-disc configuration with imposed pin rotation. Mechanism and Machine Theory, 2011. 46(11): p. 1755-1772.
30. Pogačnik, A. and M. Kalin, How to determine the number of asperity peaks, their radii and their heights for engineering surfaces: A critical appraisal. Wear, 2013. 300(1-2): p. 143-154.
31. Greenwood, J.A. and J.H. Tripp, The Contact of Two Nominally Flat Rough Surfaces. Proceedings of the Institution of Mechanical Engineers, 1967. 185(1): p. 625-633.
32. Bieberdorf, N., et al., An Evaluation of Different Plasticity and Failure Laws in Simulating Puncture in 7075-T651 Aluminum. 2018, Sandia National Lab.(SNL-NM), Albuquerque, NM (United States).
33. Corona, E. and G.E. Orient, An evaluation of the Johnson-Cook model to simulate puncture of 7075 aluminum plates. 2014, Sandia National Lab.(SNL-NM), Albuquerque, NM (United States).
34. Committee, A.H., Properties and Selection: Nonferrous Alloys and Special-Purpose Materials. 1990: ASM International.
35. United States. National Advisory Committee for, A., National Advisory Committee for Aeronautics. 1954: National Advisory Committee for Aeronautics.
36. Archard, J.F., Surface topography and tribology. Tribology, 1974. 7(5): p. 213-220.
37. Kogut, L. and I. Etsion, A Finite Element Based Elastic-Plastic Model for the Contact of Rough Surfaces. Tribology Transactions, 2003. 46(3): p. 383-390.
38. Maugis, D., On the contact and adhesion of rough surfaces. Journal of Adhesion Science and Technology, 1996. 10(2): p. 161-175.
39. Archard, J.F. and W. Hirst, The wear of metals under unlubricated conditions. Proceedings of the Royal Society of London. Series A. Mathematical and Physical Sciences, 1956. 236(1206): p. 397-410.
40. Feroz Ali, L., et al., Wear and friction properties of AA 7075-T6 with × wt% of WC surface composite fabricated by FSP technique. Materials Today: Proceedings, 2021. 45: p. 6482-6487.
41. Brizmer, V., Y. Kligerman, and I. Etsion, Elastic–plastic spherical contact under combined normal and tangential loading in full stick. Tribology Letters, 2006. 25(1): p. 61-70.